

Nanoscale

Accepted Manuscript

This article can be cited before page numbers have been issued, to do this please use: D. Coral Perez, B. Matute Rauli, S. Slimi, F. Díaz, M. Aguiló and X. Mateos, *Nanoscale*, 2026, DOI: 10.1039/D5NR05387K.



This is an Accepted Manuscript, which has been through the Royal Society of Chemistry peer review process and has been accepted for publication.

Accepted Manuscripts are published online shortly after acceptance, before technical editing, formatting and proof reading. Using this free service, authors can make their results available to the community, in citable form, before we publish the edited article. We will replace this Accepted Manuscript with the edited and formatted Advance Article as soon as it is available.

You can find more information about Accepted Manuscripts in the [Information for Authors](#).

Please note that technical editing may introduce minor changes to the text and/or graphics, which may alter content. The journal's standard [Terms & Conditions](#) and the [Ethical guidelines](#) still apply. In no event shall the Royal Society of Chemistry be held responsible for any errors or omissions in this Accepted Manuscript or any consequences arising from the use of any information it contains.

Cite this: DOI: 00.0000/xxxxxxxxxx

Floating Nanometric Poly(methyl methacrylate) Films by Bursting Bubbles

David Coral^a Beatriz Matute-Rauli^a Sami Slimi^a Francesc Diaz^a Magdalena Aguilo^a and Xavier Mateos,^{*a}Received Date
Accepted Date

DOI: 00.0000/xxxxxxxxxx

During bubble formation, a thin layer is created by the physical effects of a gas being trapped. This phenomenon is observed in polymers too, allowing the creation of a similar layer that is destroyed once bubbles collapse. Spin coating, vapor deposition, sputtering, or solution flotation are examples of techniques used to fabricate polymeric thin films using complex, expensive, or specific equipment. Additionally, manipulating thin bubble layers can be extremely hard. Here we show that polymer bubbles produced under water can create nanometer-thick polymer layers by popping them on the water surface. Our results showcase the formation of nanometric films by bursting bubbles made of polymethylmethacrylate. Moreover, we developed nanocomposite layers of equivalent thicknesses, incorporating luminescent nanoparticles. Lastly, we achieved a sensor approach by sample collection on the bubble surface within a medium through bubble dragging. We foresee a universal method in the field of polymers, including semiconductor ones, with applications in sensing, transistor manufacturing, and cationic traps for quantum computing.

Keywords: Nanofilms; Nanolayer; Bubbles; Nanocomposites; Nanofabrication

1 Introduction

For centuries, the formation and bursting of bubbles have captivated observers, as these phenomena spontaneously occur in nature. This includes instances like aquatic plants generating oxygen at a faster rate than its dissolution in water^{1,2}, the release of gases like methane from the depths of lakes^{3,4}, and even simple and artificial situations, such as blowing a chewing gum to produce a bubble⁵. Bubbles have been studied in detail from their formation to their bursting, which has driven technological advances in areas such as remediation of aquatic environments^{6–8}, drug delivery in medicine^{9,10}, bubble-up in chemical synthesis^{11,12}, and controlled mechanics in soft robotics¹³.

Despite the relevance of bubbles in nature and their thin layer^{14,15}, information regarding nanometric-thick polymeric layers from bubbles is scarce. Only theoretical¹⁶ or uncontrolled experimental¹⁷ demonstrations are found in the literature. Numerical methods describe roughly the bubble geometry, while experimental evidence produces layers with wrinkles caused during polymerization or as a consequence of the collection process, and uncontrolled thickness^{17–19}. Recent work by Qian and He

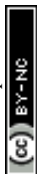
demonstrated the formation of nanoscale polymer membranes using a bubble-spinning approach, where mechanically expanded bubbles are ruptured and collected on a solid substrate. While this strategy highlights the potential of bubble-mediated thinning, it relies on externally induced deformation and results in fragmented membrane structures.¹⁷

Beyond bubbles, there are other technologies to achieve nanometric-thick polymeric layers^{20–23}. For example, spin coating creates polymeric thin layers with relevant applications (e.g. diode fabrication²⁴ and transistor manufacturing²⁵), but suffers from notable polymer loss and considerable time consumption due to solvent evaporation and baking steps.

Inspired by bubbles, we developed a simple method for crafting ultra-thin and ultra-smooth (wrinkle-free) polymeric layers using polymethylmethacrylate (PMMA) bubbles over the water surface, creating an alternative approach based on a liquid–liquid interfacial system, where polymer bubbles formed under water undergo spontaneous thinning driven by solvent evaporation and interfacial tension gradients. This process enables the formation of continuous, ultrathin, and homogeneous polymeric layers, offering improved structural control and expanding the potential of bubble-assisted nanofabrication. These layers were characterized across a wide spectrum of solvent–polymer blend concentrations, enabling controlled thickness and homogeneous roughness. In this work, we address the challenge of achieving continuous and controllable nanometric polymer films using a simple and scalable approach. We investigate how interfacial phenomena govern

^a University Rovira i Virgili (URV), Physics and Crystallography of Materials (FiCMA), Marcel·lí Domingo 1, 43007 Tarragona, Spain. E-mail: xavier.mateos@urv.cat, jesus-david.coral@urv.cat, sami.slimi@urv.cat, f.diaz@urv.cat, magdalena.aguilo@urv.cat

* Corresponding author. E-mail: xavier.mateos@urv.cat



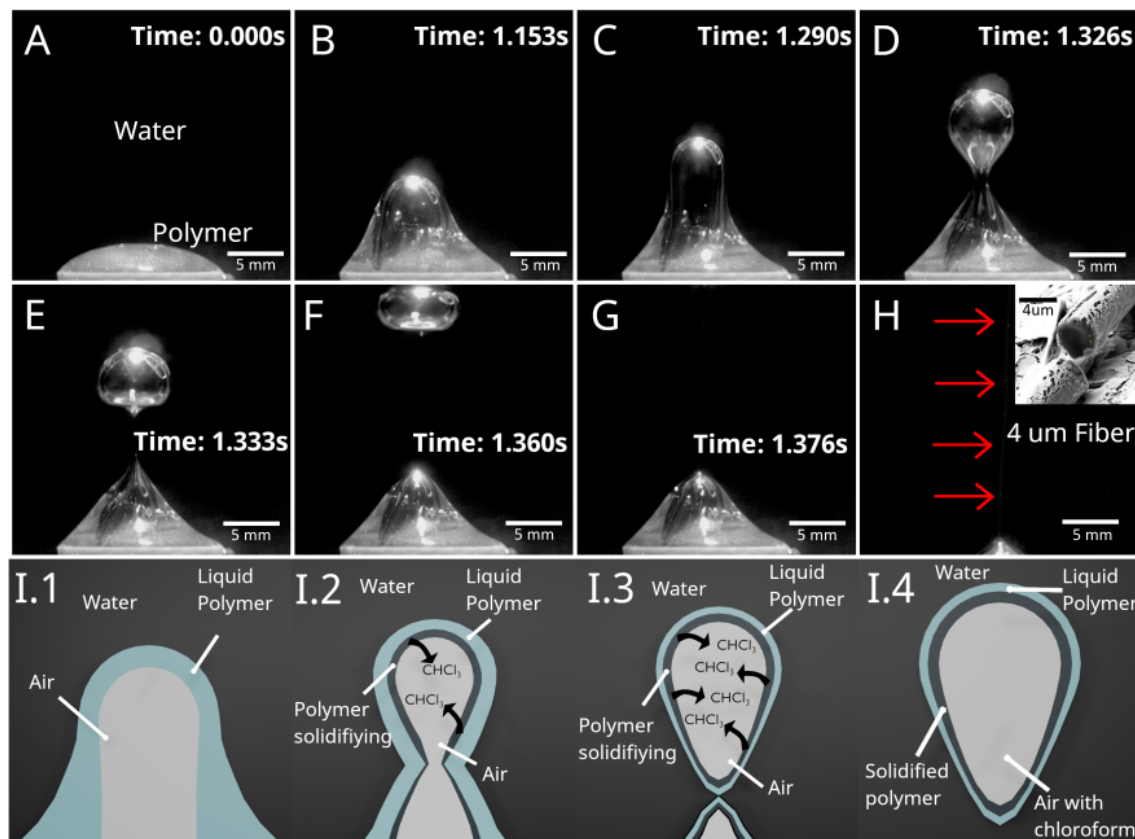


Fig. 1 Formation process of polymeric bubbles in two liquid phases (A–H). A) Start ($t = 0$): no air is introduced into the polymer. B) Air penetration into the polymer layer. C) 1.29 s after air introduction, the bubble begins to form a neck between the air volume and the polymeric body. D) 1.33 s from formation, the bubble reaches its characteristic shape. E) The interplay between water pressure and Archimedes forces tightens the neck, yielding the characteristic bubble geometry. F) The bubble rises through the water, forming a fine thread that connects it to the polymeric phase. G) The thread ruptures and the bubble fully detaches from the polymeric phase. H) Arrows indicate the presence of the polymeric fiber. Inset: Field-emission scanning electron micrograph of the polymeric fiber. (I1–I4) Artistic representation of the bubble formation. The characteristic bubble diameter is approximately 7 mm.

film formation and hypothesize that the liquid–liquid configuration enables controlled thinning prior to rupture. This hypothesis is tested through systematic variation of polymer concentration and quantitative characterization of film thickness and morphology using FESEM-FIB and TEM. Additionally, we propose two applications. The first involves creating a nanocomposite layer consisting of luminescent nanoparticles in a polymer matrix, with potential applications in wearable sensors or integrated photonic circuits. The second demonstrates dragging and collecting luminescent nanoparticles dispersed in water.

2 Results

2.1 Bubble formation

We conducted experiments with four different concentrations (1%, 5%, 10%, and 15%) of PMMA dissolved in chloroform (CHCl_3) at room temperature. In each experiment, 0.5 mL of polymer solution was deposited at the bottom of a beaker previously filled with 200 mL of Milli-Q[®] water. A bubble was formed by introducing air (0.2 mL) through a syringe into the polymer sample (see Methods, Section 3). The experiments revealed successful bubble formation within the polymer solution independently of concentration, followed by detachment into the aqueous

medium. The formation and evolution of the polymeric bubble can be interpreted in terms of capillary and viscous effects. The pressure difference across the bubble interface is governed by the Young–Laplace equation:

$$\Delta P = \frac{2\gamma}{R}$$

where γ is the surface tension and R is the bubble radius. This pressure difference controls the curvature and mechanical stability of the bubble as it forms and rises through the aqueous medium.

As the bubble evolves, the polymeric film undergoes progressive thinning. This process can be qualitatively described using lubrication theory, where the temporal evolution of the film thickness h is influenced by viscous flow and pressure gradients within the film.

In the present system, solvent evaporation plays a key role. Since chloroform preferentially evaporates into the gas phase, the polymer concentration in the film increases over time, leading to a rise in viscosity and partial solidification of the interface prior to rupture.

In Fig. 1, the bubble formation process is shown. It involves



three materials in two phases of matter (gas, liquid, and liquid). Phase one comprises trapped air. Phase two encompasses the polymer solution, and the second liquid phase is the aqueous medium. To examine and corroborate the presence of a polymer layer between the water–gas interface, a high-speed camera operating at 1350 frames per second captured the bubble formation process according to the setup explained in Supplementary material Fig. 1.

In Fig. 1A, two components are prominently observed: polymer solution and water. Fig. 1B–H illustrate bubble formation by elongation of the polymer solution, where a discernible meniscus corroborates that the bubble wall is made of liquid polymer. The geometry evolution has been described for visco-elastic materials^{26–28} and is determined by equilibrium forces including the surface tension of the three media²⁹. The surface tension of PMMA in chloroform is approximately 22–44 mN m⁻¹ depending on concentration, whereas the surface tension of water is much higher (72 mN m⁻¹), so the solvent tends to cover the aqueous interface to minimize surface energy^{30,31}. Fig. 1H shows the polymeric fiber connecting the detached bubble with the polymer source; this micrometric fiber (4 μm in diameter) is under investigation in separate work.

Fig. 1I1–I4 show an artistic representation of the time evolution of the bubble wall thickness and stability as a result of thermodynamic imbalance in the vapor pressure of chloroform³² toward the gas medium inside the bubble. Since chloroform is almost immiscible in water (only 0.8% by weight)³³, it favors evaporation into the gas phase inside the bubble rather than diffusion into water. Therefore, the inner portion of the bubble wall increases viscosity or partially solidifies throughout the bubble lifetime.

2.2 Layer formation and characterization

The rupture of the polymeric bubble and subsequent layer formation can be understood as a consequence of film instability once a critical thickness is reached. In thin liquid films, rupture is typically driven by capillary instabilities and intermolecular forces, which become dominant at nanometric thicknesses.³⁴

After rupture, the retraction and expansion of the film are driven by surface tension forces. This process can be described by the Taylor–Culick velocity:³⁵

$$v = \sqrt{\frac{2\gamma}{\rho h}}$$

where v is the retraction velocity, ρ is the density, and h is the film thickness.

In our system, the expansion of the polymeric layer over the water surface is additionally influenced by differences in interfacial tension between the polymer solution and the aqueous phase, promoting spreading and the formation of continuous films.

It is important to note that these models were originally developed for simple liquid films. In the present case, additional factors such as solvent evaporation, increasing viscosity, and the presence of a liquid–liquid–gas interface introduce further complexity. Therefore, the above framework should be understood as a qualitative approximation of the mechanisms governing bubble

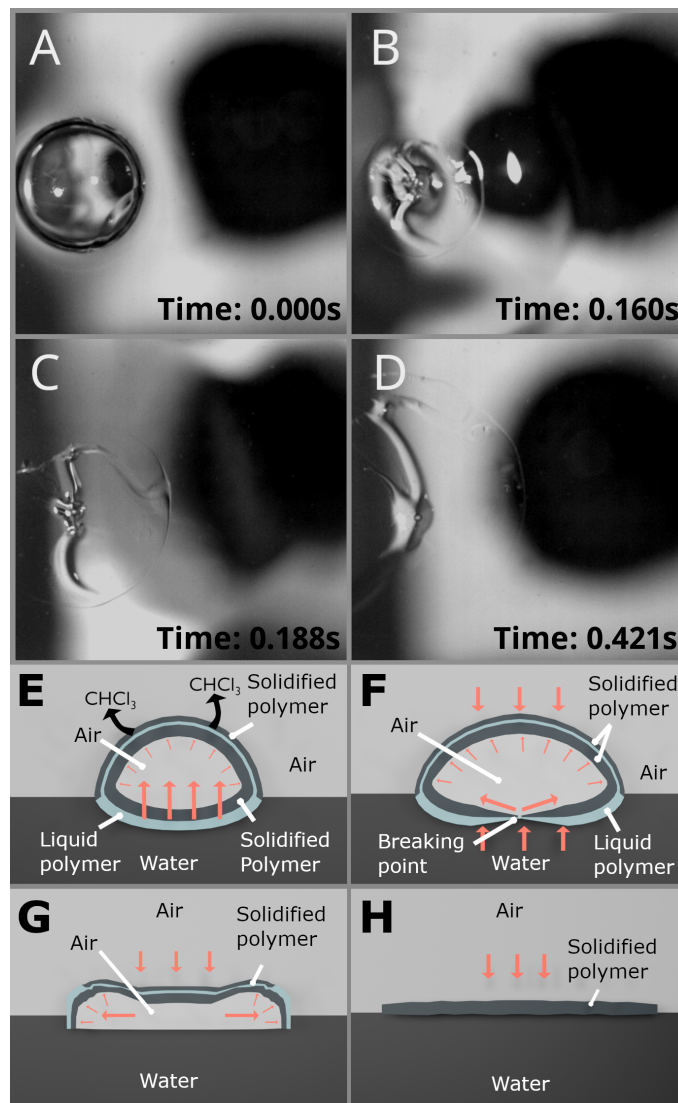
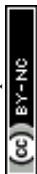


Fig. 2 Illustration showing the formation of a thin layer when a bubble bursts. A) PMMA bubble with air inside at time 0 before bursting. B) Instant when the bubble breaks at 160 ms. C) At 188 ms, the layer begins to expand. D) The polymer layer reaches maximum expansion at 421 ms. E) Artistic explanation of evaporation and solidification when the bubble emerges at the surface. F) Representation of the moment when the bubble bursts. G) Instantly, when the bubble collapses and begins expansion. H) Beginning of spreading on the water surface.

rupture and layer formation.

Bubble bursting led to thin layers on the liquid surface. Fig. 2 illustrates layer formation, supported by artistic images for clarification. At time zero (Fig. 2A), the bubble just before bursting is shown, displaying fast solidification at its surface due to solvent evaporation (see Fig. 2E–H and Supplementary Video “Bursting bubble.avi”). At 160 ms, the bubble bursts (Fig. 2B). Up to this point, the pressure of the aqueous medium on the gas volume enclosed by the polymer is greater than the external air pressure on the outer bubble surface. Consequently, the outer part toward the atmosphere solidifies faster than the submerged section, making rupture prone to initiate from the submerged region (Fig. 2F). Between 188 ms and 421 ms, differences in surface tension between



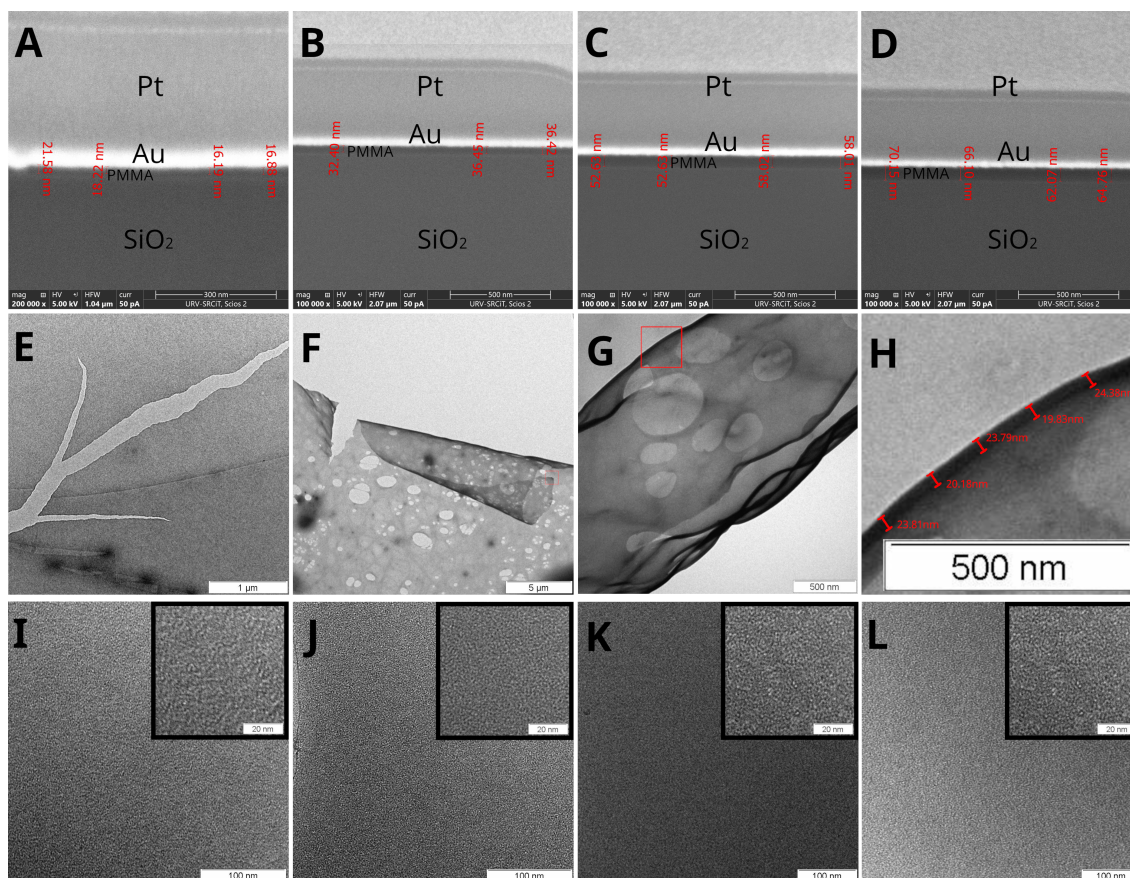


Fig. 3 A–D show cross-sections of the polymer layer at 1, 5, 10, and 15% cut and measured by FESEM-FIB. E–H show a curling-assisted thickness estimation for sample 1 (1% PMMA): E) onset of cracking; F) curling under prolonged exposure; G) coiling enabling thickness measurement; H) digital zoom with measurement. I–L show surface images at 500 nm and 20 nm scales indicating homogeneity.

water and submerged polymer drive spreading of the polymeric layer, tending to expand to cover as much aqueous surface as possible (Fig. 2G–H). In other visco-elastic bubbles (glycerine)³⁶, rupture starts at the top rather than the bottom; this particularity is not observed in PMMA bubbles here.

The fabricated layer was collected from the aqueous medium using Water-Assisted Layer Transfer, enabling deposition on diverse substrates and transfer between aqueous solutions^{37–40}.

For characterization (Methods, Section 3.2), field-emission scanning electron microscopy combined with focused ion beam (FESEM-FIB) yielded average thickness values of 18.2 ± 2.4 nm (1%, Fig. 3A), 35.1 ± 2.3 nm (5%, Fig. 3B), 55.3 ± 2.4 nm (10%, Fig. 3C), and 65.8 ± 3.4 nm (15%, Fig. 3D), showing the thickness trend with concentration. We also tested polystyrene to explore generality: 5% polystyrene in chloroform produced a 364 ± 3.8 nm layer (Supplementary material Fig. ??), consistent with its higher surface tension (63.3 mN m^{-1})³⁰ relative to PMMA ($22\text{--}44 \text{ mN m}^{-1}$).

In addition to FESEM-FIB, we propose an alternative thickness estimation using transmission electron microscopy (TEM) and digital analysis. For the 1% sample, prolonged exposure led to cracking and curling, generating regions perpendicular to the imaging plane suitable for thickness estimation (Fig. 3E–H). A maximum magnification of 500 nm (40k) at the coiled region pro-

vided an estimated thickness of 22.4 ± 2.2 nm (Fig. 3H), in good agreement with FESEM-FIB (18.2 ± 2.4 nm). TEM surface analysis (Fig. 3I–L) shows a homogeneous polymer layer even at 20 nm scale ($\times 800k$), without particulate or filamentous structures (in contrast to literature²¹), supporting a reproducible fabrication method.

It is worth noting that the morphology of the polymeric layers obtained in this work differs significantly from previously reported bubble-based membrane fabrication approaches. In bubble-spinning methods, such as that reported by Qian and He, membrane formation typically results in fragmented structures with pronounced wrinkling due to mechanical deformation and rapid rupture.

In contrast, the layers produced here are continuous and exhibit a high degree of surface homogeneity, as confirmed by TEM analysis, without the presence of wrinkles or filamentary features. This difference highlights the role of the liquid–liquid interfacial mechanism in enabling controlled and uniform nanometric film formation.

2.3 Applications

The method is applied to (a) fabrication of a layered nanocomposite and (b) dragging of nanoparticles dispersed in water.



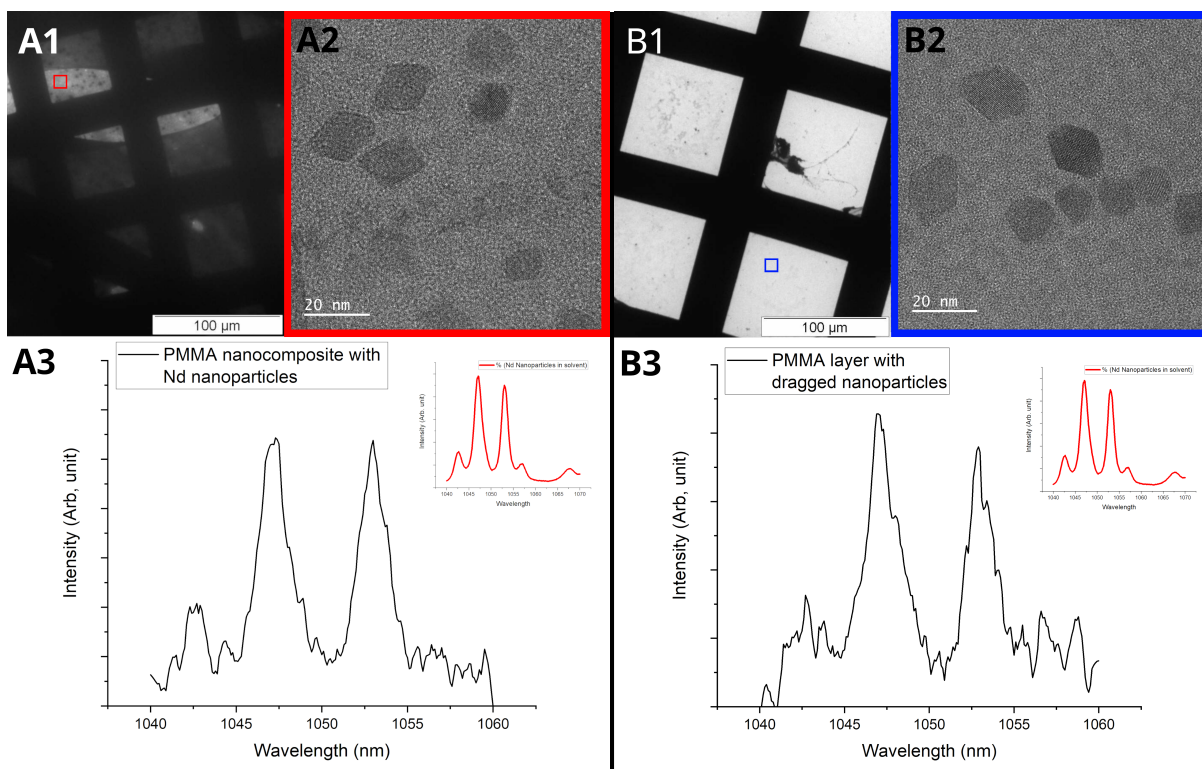


Fig. 4 A) Polymeric layers fabricated with 10% PMMA solution containing luminescent nanoparticles dispersed in chloroform. B) Polymeric layers fabricated with 10% PMMA in chloroform while the aqueous medium contained luminescent nanoparticles. A1) HRTEM image of nanocomposite layers on holey grids. A2) Nanoparticles in the nanocomposite at $\times 800k$. A3) Emission spectrum of the nanocomposite layer (inset: nanoparticle spectrum in solvent, red line). B1) Layers after dragging nanoparticles, deposited on holey grids. B2) Dragged nanoparticles at $\times 800k$. B3) Emission spectrum after dragging (inset: nanoparticle spectrum in solvent, red line).

2.3.1 Fabrication of layered nanocomposite

A nanocomposite layer (PMMA + luminescent nanoparticles) was fabricated as described in Methods (Section 3.3.1). Fig. 4A shows TEM imaging of a nanocomposite layer consisting of PMMA and neodymium-doped lithium yttrium fluoride core-shell nanocrystals (4 at.% $\text{Nd}^{3+}:\text{LiYF}_4@\text{LiYF}_4$) deposited on a holey copper grid. Sub-20 nm rhomb-shaped nanocrystals are observed at $\times 800k$ magnification (Fig. 4A2; Supplementary material Fig. ??), confirming incorporation within the polymeric nanolayer. Thickness estimation yielded ~ 53 nm, comparable to the 10% PMMA layer without nanoparticles (55.3 ± 2.4 nm), indicating reproducibility.

The Nd-doped nanoparticles absorb around 800 nm and emit between 1040 and 1060 nm (Fig. 4A3; inset shows reference emission of nanoparticles in chloroform). The nanocomposite layer was excited at 793 nm and emission was collected between 1040 and 1060 nm (Fig. 4A3), revealing characteristic Nd^{3+} bands despite the thin film thickness.

2.3.2 Dragging of nanoparticles dispersed in water

We tested dragging of specimens dispersed in the aqueous medium following Methods (Section 3.3.2), using the same Nd-doped nanoparticles dispersed in water. After bubble collapse, nanoparticles were found associated with the polymeric layer (Fig. 4B2), demonstrating an approach for depositing nanoparticles on a surface with potential sensing utility (cf. ⁴¹). The presence of nanoparticles is confirmed by morphology (Fig. 4B2) and

by emission bands (Fig. 4B3). Similar effects have been demonstrated for microscopic particles^{6,7}, but not at the nanoscale.

3 Materials and Methods

In this section, the fabrication of polymeric nanolayers is detailed, along with two application examples. Layers were fabricated using powdered polymethylmethacrylate (PMMA, Sigma-Aldrich) and chloroform (99.91% in ethanol, Sigma-Aldrich). Milli-Q[®] water (200 mL) from a Milli-Q[®] EQ 7000 system was used. For deposition, 1 mL syringes were employed. For bubble formation, a needle with an inner diameter of 0.127 mm and a 1 mL syringe were used to introduce air into the polymer solution, generating the bubble and, upon bursting, the nanolayer.

3.1 Layer fabrication

Polymeric samples dissolved in chloroform were prepared with a total volume of 5 mL each. PMMA amounts corresponding to 1%, 5%, 10%, and 15% by weight were weighed and gradually dissolved in chloroform under mechanical stirring until homogeneous solutions were obtained.

For each experiment, 0.5 mL of the polymer solution was deposited at the bottom of a beaker containing 200 mL of Milli-Q[®] water (see Fig. 5A). Bubble formation was induced by injecting approximately 0.2 mL of air using a syringe equipped with a needle of inner diameter 0.127 mm, positioning the needle tip within the polymer solution.



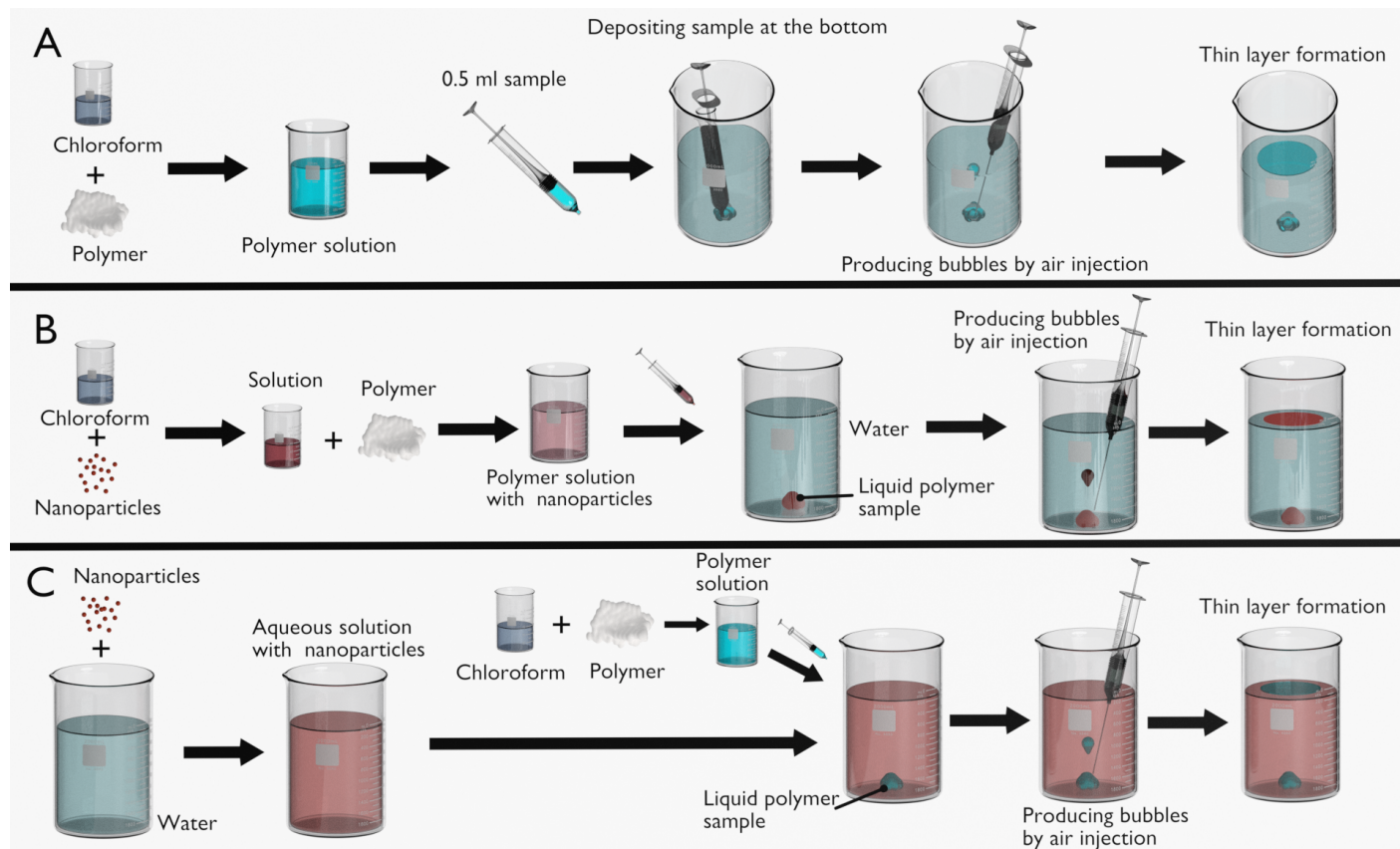


Fig. 5 Schematic representation of: A) polymeric nanolayer fabrication method; B) polymethylmethacrylate nanocomposite fabrication (PMMA + Nd-doped nanoparticles); C) dragging of Nd-doped nanoparticles dispersed in water.

All experiments were conducted at room temperature (23 °C). Upon air injection, a bubble was formed (Section 2.1), rising through the aqueous medium and generating a nanometric layer upon rupture at the water surface.

3.2 Layer characterization

Two analyses were performed to assess thickness and surface quality.

For FESEM-FIB analysis, layers were transferred onto silicon wafers and coated with a 40 nm Au layer (Spin Coating Auroa SP200) to protect the polymer surface. Selected regions were further protected with Pt prior to cross-sectioning using a focused ion beam (FIB), enabling direct thickness measurements.

For TEM analysis, layers were collected on copper holey grids and analyzed to evaluate surface morphology, structural homogeneity, and the presence of nanoscale features.

3.3 Application of the method

Two applications are shown: fabrication of layered nanocomposites as an alternative to conventional approaches (e.g. mixing⁴²), and fabrication of polymeric nanometric layers enabling targeted nanoparticle capture.

3.3.1 Fabrication of layered nanocomposite

As depicted in Fig. 5B, a 4 mM solution of neodymium-doped core-shell nanoparticles (4 at.% Nd³⁺:LiYF₄@LiYF₄) dispersed in chloroform was prepared. The nanoparticle dispersion was homogenized prior to use. The fabrication procedure followed Section 3.1, using PMMA at 10% by weight.

3.3.2 Fabrication by dragging of nanoparticles

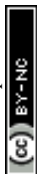
Nd-doped nanoparticles (4 mM of 4 at.% Nd³⁺:LiYF₄@LiYF₄) were dispersed in Milli-Q[®] water. To improve dispersion stability, 2 mL of acetone was added to the system.

To generate polymer bubbles free of nanoparticles, 5 mL of 10% PMMA solution was introduced into the aqueous phase containing nanoparticles. Bubble formation and subsequent rupture enabled the interaction between the polymeric layer and dispersed nanoparticles (Fig. 5C).

3.3.3 Characterization of nanoparticle-containing layers

Nanoparticle-containing layers were characterized by TEM to evaluate nanoparticle incorporation and spatial distribution.

Luminescence analysis was carried out using a fiber-coupled diode laser (BWT) operating at 793 nm to excite Nd³⁺ ions. Emission spectra were collected using an optical spectrum analyzer over the range of 1040–1070 nm.



Conclusions

In conclusion, a reproducible method for the fabrication of nanometric polymeric films based on the formation and bursting of polymer bubbles at the water surface has been demonstrated. Using polymethyl methacrylate as a model system, films with thicknesses between approximately 18 and 66 nm were obtained by varying the polymer concentration.

The resulting layers were found to be continuous across the analyzed regions (tens to hundreds of micrometers) and exhibited consistent thickness and morphology, as confirmed by FESEM-FIB and TEM analysis. At the nanometric scale, TEM observations revealed smooth surfaces without visible wrinkles, discontinuities, or particulate aggregation, supporting the claim of structural homogeneity.

These results indicate that the method enables the formation of smooth layers with controlled thickness without the need for complex fabrication equipment or additional processing steps.

Film formation is governed by solvent evaporation, surface-tension imbalance, and viscoelastic stabilization of the bubble wall, and the applicability of the method was verified through the fabrication of luminescent nanocomposite films and the collection of nanoparticles dispersed in water.

Compared to previously reported bubble-based membrane fabrication methods, the present approach introduces a fundamentally different mechanism based on liquid–liquid interfacial phenomena rather than mechanical deformation. This enables the formation of continuous, ultrathin, and structurally homogeneous polymeric films with tunable thickness.

Furthermore, the ability to incorporate functional nanoparticles and to actively collect dispersed species from the surrounding medium extends the concept beyond fabrication, positioning this method as a versatile platform for nanocomposite engineering and sensing applications.

Author contributions

D.C. and X.M. designed the research. D.C., S.S., and B.M.R. carried out the experiments. D.C. and S.S. analyzed the data. D.C., B.M.R., and X.M. wrote the paper. X.M., F.D., and M.A. acquired funding, and D.C., B.M.R., X.M., F.D., and M.A. reviewed, commented on, and approved the article.

Conflicts of interest

There are no conflicts to declare.

Acknowledgements

This project has received funding from the European Union's Horizon 2020 research and innovation programme under the Marie Skłodowska-Curie grant agreement No. 945413 and the Universitat Rovira i Virgili (URV). We acknowledge funding through Grant PID2022-141499OB-I00 funded by MCIN/AEI/10.13039/501100011033.

Notes and references

1 R. Ryplova, J. Pokorný and M. Baxa, *European Journal of Sustainable Development*, 2023, **12**, 69.

- 2 S. Maberly and D. Spence, *Aquatic Botany*, 1989, **34**, 267–286.
- 3 M. Keller and R. F. Stallard, *Journal of Geophysical Research*, 1994, **99**, 8307–8319.
- 4 M. Sasaki, S. Imura, S. Kudoh, T. Yamanouchi, S. Morimoto and G. Hashida, *Journal of Geophysical Research Atmospheres*, 2009, **114**, 1–6.
- 5 L. Martinetti, A. M. Mannion, J. Voje, William E., R. Xie, R. H. Ewoldt, L. D. Morgret, F. S. Bates and C. W. Macosko, *Journal of Rheology*, 2014, **58**, 821–838.
- 6 X. Feng and B. Zhang, *Marine Pollution Bulletin*, 2023, **194**, 115371.
- 7 B. Swart, Y. M. Chew and J. Wenk, *Chemical Engineering Research and Design*, 2023, **197**, 148–158.
- 8 Y. Cheng, N. Zhao, K. Zhang and W. Wei, *Ocean Engineering*, 2021, **232**, 1–12.
- 9 M. Ikeda, Y. Yutaka, T. F. Chen-Yoshikawa, M. Tanaka, M. Yamamoto, S. Tanaka, Y. Yamada, A. Ohsumi, D. Nakajima, M. Hamaji, A. Yoshizawa, E. Kusaka, M. Nagao and H. Date, *Scientific Reports*, 2023, **13**, 1–9.
- 10 M. Kancheva, L. Aronson, T. Pattilachan, F. Sautto, B. Daines, D. Thommes, A. Shar and M. Razavi, *Journal of Functional Biomaterials*, 2023, **14**, 7.
- 11 X. Li, H. Shi, X. Wang, X. Hu, C. Xu and W. Shao, *Journal of Alloys and Compounds*, 2022, **921**, 1–14.
- 12 Y. B. Vogel, C. W. Evans, M. Belotti, L. Xu, I. C. Russell, L. J. Yu, A. K. Fung, N. S. Hill, N. Darwish, V. R. Gonçalves, M. L. Coote, K. S. Iyer and S. Ciampi, *Nature Communications*, 2020, **11**, 1–8.
- 13 T. J. Jones, E. Jambon-Puillet, J. Marthelot and P. T. Brun, *Nature*, 2021, **599**, 229–233.
- 14 S. F. Ahmadi, S. Nath, C. M. Kingett, P. Yue and J. B. Boreyko, *Nature Communications*, 2019, **10**, 1–10.
- 15 C. Cohen, B. D. Texier, E. Reyssat, J. H. Snoeijer, D. Quéré and C. Clanet, *Proceedings of the National Academy of Sciences*, 2017, **114**, 2515–2519.
- 16 K. Park, D. Choi and J. Hong, *Scientific Reports*, 2018, **8**, 1–9.
- 17 M. Y. Qian and J. H. He, *Surfaces and Interfaces*, 2022, **28**, 1–7.
- 18 Y. J. Kim, H. T. Jung, C. W. Ahn and H. J. Jeon, *Advanced Materials Interfaces*, 2017, **4**, 1–8.
- 19 E. Bormashenko, A. Musin, Y. Bormashenko, G. Whyman, R. Pogreb and O. Gendelman, *Macromolecular Chemistry and Physics*, 2007, **208**, 702–709.
- 20 D. Tammara, V. C. Suja, A. Kannan, L. D. Gala, E. D. Maio, G. G. Fuller and P. L. Maffettone, *Proceedings of the National Academy of Sciences*, 2021, **118**, e2105058118.
- 21 Y.-J. Kim, H.-T. Jung, C. W. Ahn and H.-J. Jeon, *Advanced Materials Interfaces*, 2017, **4**, 1700342.
- 22 L. K. Sai, K. K. Swain and S. K. Pradhan, *John Wiley & Sons*, 2023, 155–177.
- 23 A. Asatekin, M. C. Barr, S. H. Baxamusa, K. K. Lau, W. Tenhaeff, J. Xu and K. K. Gleason, *Materials Today*, 2010, **13**, 26–33.



- 24 N. Matsuhisa, S. Niu, S. J. O'Neill, J. Kang, Y. Ochiai, T. Katsumata, H. C. Wu, M. Ashizawa, G. J. N. Wang, D. Zhong, X. Wang, X. Gong, R. Ning, H. Gong, I. You, Y. Zheng, Z. Zhang, J. B. Tok, X. Chen and Z. Bao, *Nature*, 2021, **600**, 246–252.
- 25 S. Han, X. Yang, X. Zhuang, J. Yu and L. Li, *Materials*, 2016, **9**, 1–10.
- 26 S. Rajesh, S. S. Peddada, V. Thiévenaz and A. Sauret, *Journal of Non-Newtonian Fluid Mechanics*, 2022, **310**, 104921.
- 27 X. Yu, Y. Wang, C. Huang and T. Du, *Journal of Physics: Conference Series*, 2015, **656**, 012042.
- 28 B. Ji, Z. Yang and J. Feng, *Nature Communications*, 2021, **12**, 1–10.
- 29 R. Bonhomme, J. Magnaudet, F. Duval and B. Piar, *Journal of Fluid Mechanics*, 2012, **707**, 405–443.
- 30 *Comprehensive Tables*, ed. D. Van Krevelen and K. Te Nijenhuis, Elsevier, Amsterdam, Fourth Edition edn, 2009, pp. 889–953.
- 31 E. Bormashenko, A. Musin, Y. Bormashenko, G. Whyman, R. Pogreb and O. Gendelman, *Macromolecular Chemistry and Physics*, 2007, **208**, 702–709.
- 32 C. Schaefer, P. V. D. Schoot and J. J. Michels, *Physical Review E - Statistical, Nonlinear, and Soft Matter Physics*, 2015, **91**, 1–6.
- 33 H. S. Hu, *Fluid Phase Equilibria*, 2010, **289**, 80–89.
- 34 J. N. Israelachvili, *Intermolecular and Surface Forces*, Academic Press, 3rd edn, 2011.
- 35 F. E. C. Culick, *Journal of Applied Physics*, 1960, **31**, 1128–1129.
- 36 A. Oratis, J. Bush, H. Stone and J. Bird, *Science*, 2020, **369**, 685–688.
- 37 J. H. Kim, T. J. Ko, E. Okogbue, S. S. Han, M. S. Shawkat, M. G. Kaium, K. H. Oh, H. S. Chung and Y. Jung, *Scientific Reports*, 2019, **9**, 1–10.
- 38 A. Chauvin, W. T. C. Heu, J. Buh, P. Y. Tessier and A. A. E. Mel, *npj Flexible Electronics*, 2019, **3**, 1–6.
- 39 H. V. Ngoc, Y. Qian, S. K. Han and D. J. Kang, *Scientific Reports*, 2016, **6**, 1–9.
- 40 M. Sledzinska, B. Graczykowski, M. Placidi, D. S. Reig, A. E. Sachat, J. S. Reparaz, F. Alzina, B. Mortazavi, R. Quey, L. Colombo, S. Roche and C. M. S. Torres, *2D Materials*, 2016, **3**, 035016.
- 41 A. S. Roy, *Sensors and Actuators A: Physical*, 2018, **280**, 1–7.
- 42 L. woon Jang, J. Lee, E. Razu, E. C. Jensen and J. Kim, *IEEE Transactions on NanoBioscience*, 2015, **14**, 841–849.



Data Availability Statement

The data supporting this study “**Floating Nanometric Poly(methyl methacrylate) Films by Bursting Bubbles**” are available within the article and its Supplementary Information. Additional data are available from the corresponding author upon reasonable request.

